A&A 397, 1083–1095 (2003)
DOI: 10.1051/0004-6361:20021549

Astronomy & Astrophysics

Dynamics of solar coronal loops

L. Di G. Sigalotti[1] and C. A. Mendoza-Briceño[2,3]

[1] Instituto Venezolano de Investigaciones Científicas, IVIC, Apartado 21827, Caracas 1020A, Venezuela
[2] Centro de Astrofísica Teórica, CAT, Facultad de Ciencias, Universidad de Los Andes, Apartado Postal 26, La Hechicera, Mérida 5251, Venezuela
e-mail: cesar@ciens.ula.ve
[3] Department of Applied Mathematics, University of Sheffield, Hicks Building, Hounsfield Road, S3 7RH, England, UK
e-mail: c.mendoza@sheffield.ac.uk

Received 8 April 2002 / Accepted 23 October 2002

Abstract. Observations in X-ray and EUV of the solar corona reveal the existence of very complex and dynamic structures made of plasma magnetically confined in loops. These structures can be studied by means of one-dimensional hydrodynamical loop models. Here we use a Lagrangian-remap code to simulate the dynamics of solar coronal loops with the purpose of quantifying the effects of varying the initial distribution of energy along the loop, the amount of input heating (h_0), the total loop length ($2L$) and including/excluding the solar gravity term. In particular, the model calculations with no gravity are compared with the results obtained from previous isobaric, time-dependent models. Using a heat function that depends on distance along the loop and temperatures at the base of the loop typical of the solar corona, we find that in the non-gravity cases the plasma is allowed to cool down to chromospheric temperatures only when the decay length of the heating is below a certain critical value ($s_H/L = 0.043$). For the same initial parameters, the inclusion of gravity produces final equilibrium states which are considerably hotter than those obtained when gravity is neglected and lowers the critical value of the decay length of the heating for which a cool condensation forms. In all cases, the outcome of the evolution can be predicted by a diagnostic diagram which describes the location of possible solutions for thermal equilibrium models.

Key words. hydrodynamics – methods: numerical – Sun: atmosphere – Sun: prominences – Sun: corona

1. Introduction

High resolution observations show that the solar corona is highly structured, where the building blocks are loops. These loops are closed magnetic flux tubes confining X-ray emitting plasma. Many basic loop properties were first learnt from Skylab, revealing a time-variable X-ray corona. In addition, the Solar Maximum Mission provided observations of the spatial structure of the transition region and details of the flows in it. However, with their better resolution YOHKOH, SOHO and TRACE have completely transformed the view of loops, showing them to be much more dynamic (Tsuneta 1993; Strong 1994; Nightingale et al. 1999). Despite this new observational findings the vast majority of the loops appear relatively steady on the basis of their characteristic times.

Theoretical work on the physics of solar corona has mainly focused on studying the structure, heating and dynamics of coronal material. Since coronal loops are often seen to possess lifetimes which are greater than the timescales defined by thermal conduction and radiation losses, several authors have studied their thermal structure by means of hydrostatic equilibrium models (Rosner et al. 1978; Hood & Priest 1979; Vesecky et al. 1979; Serio et al. 1981; Hood & Anzer 1988; Steele & Priest 1994; Mendoza-Briceño & Hood 1997 and references therein). Recently, Lenz et al. (1999) studied the temperature and emission-measure distributions along four steady loops observed with TRACE at the limb of the Sun, finding essentially no temperature variation along them. They further compared the observed loop structure with isothermal and nonisothermal static models. Furthermore, Oluseyi et al. (1999) considered quasi-static loop models using initial conditions motivated by the observations. They found three general classes of solutions, namely, radiation-dominated loops, conduction-dominated loops and classical loops. An important conclusion from their work is that a steady state solution with a uniform heating function is not consistent with the observational data. More recently, Landini & Landi (2002) considered quasi-static and isobaric models with variable loop section. They developed a simple diagnostic procedure to compare the relevant physical properties of the models with a set of spectral observations

Send offprint requests to: L. Di G. Sigalotti,
e-mail: lsigalot@cassini.ivic.ve

of loops as obtained by the CDS and SUMER instruments of SOHO. Recent observations of coronal loops in EUV wavelengths with TRACE and SOHO/EIT demonstrated that these are near-isothermal along their coronal segments and that they show an overpressure compared with models of steady state loops with uniform heating. Aschwanden et al. (2001) fitted for the first time steady state solutions of the hydrodynamic equations to the observed intensity profiles, finding that the observed loops are inconsitent with uniform heating and also with the requirement of hydrostatic equilibrium.

One-dimensional (1D) fluid dynamic models of solar coronal loops have been considered by several authors (e.g., Mariska 1987; Klimchuk 1987; Klimchuk & Mariska 1988; Mok et al. 1990; Brown 1996; Antiochos et al. 1999; Sarro et al. 1999; Teriaca et al. 1999; Reale et al. 2000). In particular, Antiochos et al. (1999) have simulated the formation of a prominence condensation in a coronal loop. With their adaptive code, they were able to follow the onset of the condensation and the subsequent evolution, with the formation of shock fronts and steep transition regions between the condensation and the rest of the corona. Moreover, Reale et al. (2000) performed simulations of a loop brightening as observed with TRACE at a high angular and temporal resolution, yielding insight on the timing and location of the heating in the loop. For deeper insight into the basic ideas underlying 1D simulations of coronal loops, the reader is referred to the recent review by Peres (2000).

Unlike most previous work, this paper deals with 1D hydrodynamical simulations of loop models with the purpose of studying the effects of (a) varying the energy distribution along the loop for models with and without the solar gravity term included, (b) varying the amount of input heating into the loop and the loop length for models with the solar gravity term included and (c) comparing the dynamical evolution with the results obtained for previous isobaric, time-dependent models (Mendoza-Briceño 1996; Mendoza & Hood 1996 hereafter MH; Mendoza-Briceño & Hood 1997). In Sect. 2 we present the governing equations and describe the loop models. The numerical techniques employed to solve these equations along with some significant tests are described in Sect. 3. The results of the hydrodynamical models are presented in Sect. 4 and Sect. 5 contains the conclusions.

2. Basic equations and models

The magnetic field plays an important role in the solar corona, producing in it a complex network of individual loop-like structures. The coronal plasma β is much smaller than unity (with typical values of $\sim 10^{-2}$) and the velocities are less than the Alfvén speed. Therefore, it can be assumed that a strong magnetic field confines the plasma in such a way as to provide a symmetric loop geometry that channels both the mass flow and the heat flux. Thus, in a first approximation, motion of the plasma along the confining magnetic field can be described by solving the equations of hydrodynamics in one-space dimension. Defining the spatial variable s as the position along a loop of constant cross-sectional area, the mass, momentum, and energy conservation equations, including radiative cooling and heating, thermal conduction, and gravity, reduce to

$$\frac{\partial \rho}{\partial t} + \frac{\partial (\rho v)}{\partial s} = 0, \tag{1}$$

$$\frac{\partial (\rho v)}{\partial t} + \frac{\partial (\rho v^2)}{\partial s} = -\frac{\partial p}{\partial s} - \rho g_{\parallel}(s), \tag{2}$$

$$\frac{\partial (\rho T)}{\partial t} + \frac{\partial (\rho v T)}{\partial s} = -\frac{\bar{\mu}(\gamma - 1)}{\mathcal{R}_{\rm g}} \left[p \frac{\partial v}{\partial s} + \mathcal{L}(\rho, T, s) - \frac{\partial}{\partial s} \left(\kappa \frac{\partial T}{\partial s} \right) \right], \tag{3}$$

where ρ is the (mass) density, v is the fluid velocity along a fixed magnetic field line, T is the temperature, p is the gas pressure, $\mathcal{R}_{\rm g}$ is the gas constant, $\gamma(=5/3)$ is the ratio of specific heats, and $\kappa = \kappa_{\parallel} \approx 10^{-11}\, T^{5/2}$ Wm^{-1} K^{-1} is the coefficient of thermal conductivity parallel to the magnetic field (Braginskii 1965). Equations (1)–(3) can be solved in closed form for given initial and boundary conditions once a constitutive relation for the pressure is specified. Here we assume an equation of state (EOS) of the form

$$p = \frac{\mathcal{R}_{\rm g}}{\bar{\mu}} \rho T, \tag{4}$$

where $\bar{\mu}$ denotes the mean molecular weight.

The gravitational acceleration $g_{\parallel}(s)$ is assumed to depend only on position along the loop and is given by

$$g_{\parallel}(s) = -g_{\odot} \cos \left[\frac{\pi}{2} \frac{(L - s)}{L} \right] = -g_{\odot} \sin \left(\frac{\pi s}{2L} \right), \tag{5}$$

where $g_{\odot} = 2.7 \times 10^4$ cm s^{-2} is the solar gravity. In particular, this form implies loops of semi-circular shape only and specifies the component of the gravitational force along the magnetic field. At the summit $s = 0$, $g_{\parallel}(0) = 0$, while at the footpoint $s = L$, $g_{\parallel}(L) = -g_{\odot}$.

The radiative loss-gain function $\mathcal{L}$ on the right-hand side of Eq. (3) is in general given by the expression

$$\mathcal{L}(\rho, T, s) = \rho^2 Q(T) - H(s, t), \tag{6}$$

where $Q(T)$ is the optically thin energy loss function and $H(s, t)$ is the unknown coronal heating term. For the present models, $Q(T)$ is approximated by a piecewise continuous function of the form

$$Q(T) = \chi T^{\alpha}, \tag{7}$$

where χ and α are radiative loss coefficients (Hildner 1974), which take constant values within particular ranges of temperature of the piecewise fitting (see Table 1). Furthermore, since the mechanism of coronal heating is not known, the heating function is assumed to have the form

$$H(s, t) = H(s) = h_0 \exp \left[-\frac{(L - s)}{s_H} \right] \tag{8}$$

for $0 \le s \le L$. Here h_0 is the heating deposition at the base ($s = L$) of the loop, s_H is the spatial decay-length of the heating source, and L is half the length of the loop measured from $s = 0$ (at the top) to $s = L$ (at the base). This form of the heating

Table 1. Hildner's (1974) cooling function coefficients and exponents.

Temperature (K)	χ	α
$<1.5\times10^4$	4.92×10^{-54}	7.4
1.5×10^4–8.0×10^4	1.20×10^{-30}	1.8
8.0×10^4–3.0×10^5	8.00×10^{-22}	0.0
3.0×10^5–8.0×10^5	3.94×10^{-8}	−2.5
8.0×10^5–10^7	5.51×10^{-17}	−1.0

mechanism represents waves that are damped in the corona so that the amount of energy supplied to the loop will decay from the base towards the summit over some spatial scale small compared to the loop length and specified by the parameter s_H. In the sequences of calculations where h_0 is kept as a fixed parameter, its value is taken to be $h_0 = 10^{-3}$ erg cm^{-3} s^{-1} (Bray et al. 1991). This value is chosen to balance the total heat input with the total energy losses in a loop model when the heating is considered to be uniform (large s_H/L) along the loop (see Sect. 4).

Integrating the heating function in Eq. (8) over half the loop length gives

$$H_{\rm t} = h_0 s_* \left[1 - \exp\left(-\frac{1}{s_*}\right)\right] , \tag{9}$$

where $s_* = s_H/L$ and $H_{\rm t}$ is the total energy input per unit length. Note that for uniform heating ($s_* \to \infty$), $H_{\rm t} \to h_0$. Thus, varying s_* and keeping h_0 and L fixed implies defining a sequence of calculations with non-constant total input heating. Similarly, holding s_* fixed and varying h_0 also produces a sequence of loop models with varying total input heating $H_{\rm t}$. However, we can also define sequences of models where the three parameters s_*, h_0 and L are varied such that $H_{\rm t}$ remains constant along them. The difference between considering constant and non-constant total heating has been discussed by Mendoza-Briceño & Hood (1997) for the case of static loop models in equilibrium. In particular, they found that for the same s_* a sequence of models with constant total energy input will evolve towards final top temperatures slightly higher compared to a non-constant total heating sequence, with the trends of the evolution being similar in both cases. Since we do not expect significant differences between the dynamical evolution of loops with a constant and non-constant total energy input, here we shall only consider variations of s_*, h_0 and L such that H_t is not constant to facilitate comparison with previous static and time-dependent models for which the inertial terms in Eqs. (1)–(3) were neglected.

The set of Eqs. (1)–(4), together with the definitions (5)–(8), can be solved for given initial and boundary conditions. The initial conditions are specified by setting the density, velocity, and temperature profiles at $t = 0$, i.e.,

$$\rho_{\rm i} = \rho(s,0);\ v_{\rm i} = v(s,0);\ T_{\rm i} = T(s,0), \tag{10}$$

with $v(s,0)$ usually taken to be zero. The values of the initial parameters used in our model calculations are given in Sect. 4. In all cases, the boundary conditions are defined by keeping the density and temperature at the base ($s = L$) of the loop constant in time and equal to the corresponding initial values, that is, $\rho(L,t) = \rho(L,0)$ and $T(L,t) = T(L,0)$ for $t \geq 0$. Given the EOS (4), this is equivalent to set a constant-pressure boundary condition at the footpoint. Here we restrict ourselves to study only symmetric loops in which the location of the summit is held fixed in space and time. Therefore, at $s = 0$ we apply reflective boundary conditions by setting

$$v(0,t) = 0;\ \frac{\partial\rho}{\partial s}(0,t) = \frac{\partial T}{\partial s}(0,t) = 0, \tag{11}$$

for $t \geq 0$. This means that the density and temperature at the summit are evolved in such a way as to always keep their spatial derivatives there identically zero.

3. Computational methods

3.1. Numerical techniques

We have developed a 1D code which is an extension of the Lagrangian-remap scheme introduced by Lufkin & Hawley (1993). In general, it solves the equations of hydrodynamics for a self-gravitating, reacting fluid including the effects of viscosity, thermal conduction, cooling and heating, generation of chemical species and net reaction rate. Here we describe the methods employed in a simplified version of the code for solving Eqs. (1)–(4) and give a brief account of some of the tests that have been made to validate its accuracy.

The code solves Eqs. (1)–(3) written in Lagrangian integral form through the use of second-order, finite-difference (FD) methods on a non-staggered mesh in which all fluid variables are assigned to the cell centers. Temporal second-order accuracy is also achieved by solving the Lagrangian equations in a predictor-corrector fashion. Both the predictor and corrector steps rely on a multistep procedure to advance the solution. This amounts to operationally splitting the source contributions so that the final update through a given timestep involves a sequence of separate substeps in which the fluid variables are partially updated. The following splitting of the source terms is used:

$$\frac{\rm d}{{\rm d}t}\int_s \rho v {\rm d}s = -\int_s \left(\frac{\partial p}{\partial s} + \rho g_{\parallel}(s)\right){\rm d}s, \tag{12}$$

$$\frac{\rm d}{{\rm d}t}\int_s \rho T {\rm d}s = -\frac{\bar{\mu}(\gamma-1)}{\mathcal{R}_{\rm g}}\int_s \mathcal{L}(\rho,T,s){\rm d}s, \tag{13}$$

$$\frac{\rm d}{{\rm d}t}\int_s \rho T {\rm d}s = \frac{\bar{\mu}(\gamma-1)}{\mathcal{R}_{\rm g}}\int_s \frac{\partial}{\partial s}\left(\kappa\frac{\partial T}{\partial s}\right){\rm d}s, \tag{14}$$

$$\frac{\rm d}{{\rm d}t}\int_s \rho T {\rm d}s = -\frac{\bar{\mu}(\gamma-1)}{\mathcal{R}_{\rm g}}\int_s p\frac{\partial v}{\partial s}{\rm d}s, \tag{15}$$

where the spatial integration is over the size Δs of a given grid-zone. The continuity Eq. (1) reduces to the mass conservation statement

$$\frac{\rm d}{{\rm d}t}\int_s \rho {\rm d}s = 0. \tag{16}$$

Consistency with the original momentum and internal energy equations is recovered by summing up the temporal derivatives in Eqs. (12)–(15). The above ordering for solving the "substep"

equations was found to produce robust and stable solutions for a large variety of test calculations. In this way, Eq. (12) is first solved explicitly by evaluating the fluid acceleration according to

$$a_i^n = -\frac{1}{\rho_i^n}\left(\frac{\partial p}{\partial s}\right)_i^n - g_{\parallel}(s_i^n), \tag{17}$$

so that new Lagrangian positions and velocities are obtained using the following simple scheme

$$\begin{aligned} s_i^{n+1} &= s_i^n + \Delta t\left(v_i^n + \frac{1}{2}\Delta t a_i^n\right), \\ v_i^{n+1} &= v_i^n + \Delta t a_i^n, \end{aligned} \tag{18}$$

where the superscripts denote the time level (i.e., $t^{n+1} = t^n + \Delta t$) and the subscripts are used to label the zone-centered positions. The stability of Eqs. (18) is highly increased by evaluating the pressure gradients in Eq. (17) by means of a cubic spline interpolation scheme. This was necessary to improve the quality of the density, pressure, and velocity profiles in loop calculations with fixed boundary conditions at the footpoint. An identical sequence to (17) and (18) is also employed in the corrector part with the only change being that the acceleration a_i^n is now replaced with its time-centered value $a_i^{n+1/2}$.

The effects of cooling and heating are next evaluated by using appropriate FD replacements to Eq. (13). Because of the non-linear dependence of the function $\mathcal{L}$ with temperature for most applications, a method analogous to those employed for solving stiff ordinary differential equations has been used here. In particular, a modified version of the semi-implicit extrapolation method of Bader & Deuflhard (1983) has been implemented (e.g., Press et al. 1992). This method is fully second-order accurate in space and time and converts Eq. (13) into the FD form

$$\delta T_i^{n+1/2} = \delta T_i^n + 2\left[1 - \frac{\Delta t}{2c_{\rm v}}\left(\frac{\partial \mathcal{L}}{\partial T}\right)_i^{n+1/2}\right]^{-1} \times\left[\frac{\Delta t}{2c_{\rm v}}\mathcal{L}_i^{n+1/2} - \delta T_i^n\right], \tag{19}$$

where $c_{\rm v} = \mathcal{R}_{\rm g}/[\bar{\mu}(\gamma-1)]$ is the specific heat at constant volume. A partially updated temperature for the effects of cooling and heating then follows from

$$T_i^{n+1} = T_i^{n+1/2} + \delta T_i^{n+1/2}. \tag{20}$$

This method involves knowledge of the density and temperature at the intermediate time level $n + 1/2$, which are obtained by first predicting updated temperatures through the use of a semi-implicit Euler scheme for solving Eq. (13) and then by linearly interpolating according to $T^{n+1/2} = (T^{n+1,p} + T^n)/2$. Time-centered densities are calculated from mass conservation by using $\rho^{n+1/2} = (\rho^n \Delta s^n)/\Delta s^{n+1/2}$, where Δs denotes the size of a particular grid-zone. When the form of the heating and cooling function (6) is known analytically the terms $(\partial\mathcal{L}/\partial T)$ in the FD replacement (19) are obtained in exact form, while for tabulated dependences of $\mathcal{L}$ with the temperature an interpolation scheme may be required to evaluate the derivatives.

The effects of thermal conduction are next quantified by solving Eq. (14) implicitly. A fully implicit integration scheme is necessary to obviate the severe timestep restrictions imposed by the diffusive nature of this term. This is accomplished by first integrating Eq. (14) over the cell size Δs to yield the FD representation

$$\begin{aligned} \frac{c_{\rm v}T_i^{n+1} - c_{\rm v}T_i^n}{\Delta t/2} &= \left(\frac{\kappa_i + \kappa_{i+1}}{\rho_i \Delta s_i}\right)\left(\frac{T_{i+1} - T_i}{\Delta s_{i+1}}\right) \\ &- \left(\frac{\kappa_i + \kappa_{i-1}}{\rho_i \Delta s_i}\right)\left(\frac{T_i - T_{i-1}}{\Delta s_i}\right), \end{aligned} \tag{21}$$

where now the superscript n is used to denote quantities at the end of the heating and cooling substep and the term on the right-hand side is meant to be time centered. Since the temperature enters as $T^{5/2}$ in the definition of κ, linearization of the above FD equation is obtained by expanding the updated temperature to first order as

$$T^{n+1} \approx T^{(n)} + \delta T^{(n)}, \tag{22}$$

such that the time centered values of the temperature and coefficient of thermal conductivity become

$$\begin{aligned} T &= \frac{1}{2}\left(T^n + T^{(n)} + \delta T^{(n)}\right), \\ \kappa &= \frac{1}{2}\left(\kappa^n + \kappa^{(n)} + \frac{5}{2}\kappa^{(n)}\frac{\delta T^{(n)}}{T^{(n)}}\right), \end{aligned} \tag{23}$$

respectively. Substitution of these values into the right-hand side of Eq. (21) leads to a set of linear algebraic equations of the form

$$-A_i^{(n)}\delta T_{i+1}^{(n)} + B_i^{(n)}\delta T_i^{(n)} - C_i^{(n)}\delta T_{i-1}^{(n)} = D_i^{(n)}, \tag{24}$$

that must be solved iteratively for the temperature variation $\delta T_i^{(n)}$. A tridiagonal matrix algorithm is used for solving this set of linear equations efficiently. Once $\delta T^{(n)}$ is calculated for each computational zone, a new temperature profile follows from $T^{(n+1)} = T^{(n)} + \delta T^{(n)}$. This process is repeated m times until $\delta T^{(m)} \to 0$, in which case $T^{n+1} = T^{(m)}$ is the final updated temperature. Finally, compressional work on the gas is performed by solving Eq. (15). Using the EOS (4), the FD representation of this equation can be easily integrated to yield

$$T_i^{n+1} = T_i^n \exp\left\{-\Delta t(\gamma - 1)\left[\nabla \cdot \boldsymbol{v}\right]_i^{n+1/2}\right\}, \tag{25}$$

where T_i^n now refers to the updated temperature from the thermal conduction substep. This form has the advantage of guaranteeing a positive temperature provided that the updates from all previous substeps are also positive.

After the Lagrangian update has been obtained, the solution is remapped back onto an Eulerian grid, which can be either fixed or moving, by assuming piecewise-linear representations of the fundamental variables to preserve the second-order accuracy of the Lagrangian solution. The remap equations for the density, velocity, and specific internal energy are constructed directly from the laws of mass, momentum, and energy conservation. In particular, the FD remap equation for the density is

$$\begin{aligned} \rho_i^{n+1,\rm E}\Delta s_i^{n+1,\rm E} &= \rho^{n+1,\rm L}\Delta s_i^{n+1,\rm L} \\ &- \Delta m_{i+1/2} + \Delta m_{i-1/2}, \end{aligned} \tag{26}$$

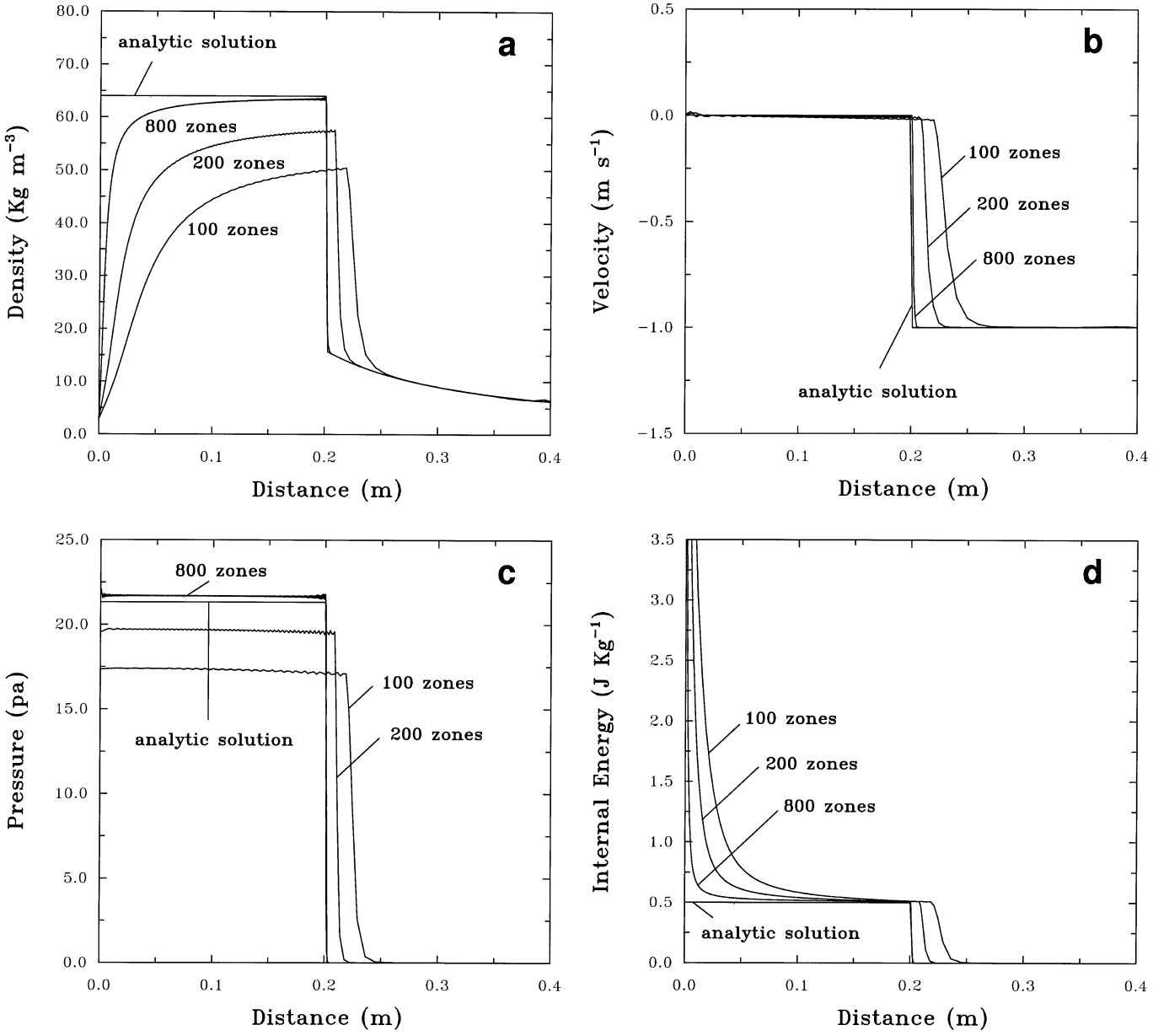

Fig. 1. Numerical solutions for Noh's spherical shock problem compared with the analytic solution at $t = 0.6$ s with 100, 200 and 800 grid-zones. The resulting profiles for the density are shown in **a)**, for the velocity in **b)**, for the pressure in **c)** and for the specific internal energy in **d)**.

where the superscripts $n+1$,E and $n+1$,L stand for the remapped Eulerian and Lagrangian updates, respectively, and $\Delta m_{i\pm1/2}$ refers to the mass contained between cell surfaces of Lagrangian and Eulerian zones. For instance, to second-order spatial accuracy $\Delta m_{i-1/2}$ is given by the product $\rho(s_{i-1/2})(s^{\rm L}_{i-1/2} - s^{\rm E}_{i-1/2})$, where $\rho(s_{i-1/2})$ obeys the upwind interpolation scheme

$$\rho(s_{i-1/2}) = \rho^{n+1,{\rm L}}_{i-1} + (s_{i-1/2} - s^{n+1,{\rm L}}_{i-1})\left(\frac{\partial\rho}{\partial s}\right)^{n+1,{\rm L}}_{i-1}, \quad (27)$$

if $s^{n+1,{\rm L}}_{i-1/2} > s^{n+1,{\rm E}}_{i-1/2}$, and

$$\rho(s_{i-1/2}) = \rho^{n+1,{\rm L}}_{i} + (s_{i-1/2} - s^{n+1,{\rm L}}_{i})\left(\frac{\partial\rho}{\partial s}\right)^{n+1,{\rm L}}_{i}, \quad (28)$$

otherwise. The slopes appearing in the above prescriptions are evaluated using the harmonic mean introduced by van Leer (1977) and limited to maintain local monotonicity in the density. A similar remap formulation is used for the velocity v and specific internal energy $e = c_{\rm v}T$. Since the Eulerian grid can be allowed to move following as close as possible the Lagrangian distortions, the remap procedure is adaptive in nature.

In order to guarantee entropy generation in the presence of shocks and spread them over a fixed number of zones, the code employs the same scalar formulation for the artificial viscosity introduced by Lufkin & Hawley (1993). The artificial viscosity is always applied after completion of the remap step. In this formulation, the artificial viscosity is chosen to scale the second derivative of the velocity so that dissipation is produced

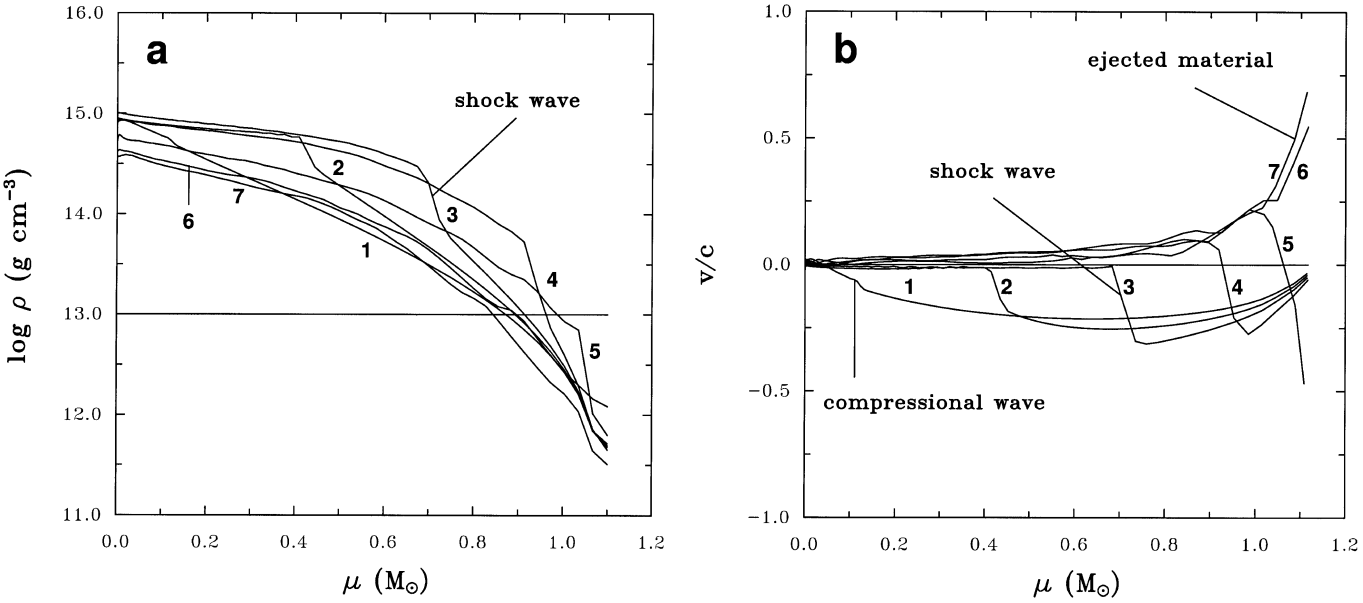

Fig. 2. a) Density and **b)** velocity profiles showing the implosion and bounce of a 1.10 $M_\odot$ neutron sphere as calculated with the code using 100 grid-zones. A sequence in time is presented: 6.5×10^{-4} s (curve 1), 6.9×10^{-4} s (curve 2), 7.3×10^{-4} s (curve 3), 8.0×10^{-4} s (curve 4), 9.0×10^{-4} s (curve 5), 1.01×10^{-3} s (curve 6) and 1.08×10^{-3} s (curve 7). The outward propagation of the shock wave is evident, and the details of the evolution compare qualitatively well with the general relativistic calculation of May & White (1966).

precisely where it is needed. This assumption also yields an artificial viscosity which vanishes under uniform compression and preserves other desirable properties as guaranteed by other existing formulations.

3.2. Tests

In addition to this Cartesian-like version, a spherical-coordinate version of the code has also been written. Both versions have been successfully tested on a large variety of problems including the standard Riemann shock tube (Sod 1978), the propagation of a shock wave in both planar and spherical geometry (Noh 1987), the collapse of a protostellar gas cloud (Sigalotti & Klapp 2001), and the implosion of a neutron star (May & White 1966). Here, we shall only describe the results of some of the more significant tests.

3.2.1. Noh's spherical shock problem

Noh's strong shock propagation in spherical geometry is known to be a severe test. Indeed, serious errors (up to 1000%) appear in the solution due to excess shock heating at the center (wall heating). Noh (1987) showed that this type of error depends on the formulation of the artificial viscosity (Q). However, the wall-heating error seems to be inevitable in FD calculations since it is already implicit in the exact solution of the differential equations when Q is added. While this conclusion holds for any shock-smearing method, it is possible to effectively eliminate the wall-heating error by adding to an appropriate Q-formulation an artificial heat transfer term H (Bae & Lahey 1999). Here we only use the scalar Q-formulation of Lufkin & Hawley (1993) with $H = 0$, and compare the results with the analytic solution.

For this test, the initial conditions consist of a sphere of radius $R = 1$ m, density $\rho = 1$ kg m^{-3}, specific internal energy $e = 0$ and pressure $p = \frac{2}{3}\rho e = 0$. The velocity everywhere is taken to be $v = -1$ m s^{-1}, except at the origin ($r = 0$) where $v = 0$. Figures 1a–d show the density, velocity, pressure and specific internal energy profiles at $t = 0.6$ s as obtained with the code working in Lagrangian mode and using an artificial viscosity coefficient $C_Q = 4$. The solution is compared with Noh's analytic solution for runs with 100, 200 and 800 computational zones. The wall heating error evident in Fig. 1d causes the central density to deviate substantially from the expected analytic value $\rho = 64$ kg m^{-3}. We note that the shock position as well as the preshock solution are very well reproduced by the 800 zones calculation. Many previous calculations for this test using either conventional FD schemes or Godunov-type methods have given comparable solutions to the one presented here. As shown by Bae & Lahey (1999), working with a better $Q\&H$ shock-following formulation, the occurrence of the wall-heating error can eventually disappear.

3.2.2. Collapse of a neutron star

May & White (1966) performed spherically symmetric calculations of the general relativistic (gravitational) collapse of cold neutron stars for varying masses and EOSs. In particular, for a hard core high-density-neutron EOS,

$$p = \frac{2}{3}\rho e, \tag{29}$$

for $\rho < \rho^\star$, and

$$p = \left(\rho - \rho^\star\right) e + \frac{2}{3}\rho^\star e, \tag{30}$$

for $\rho > \rho^\star$, with $\rho^\star = 5.0 \times 10^{14}$ g cm^{-3}, they followed the implosion and bounce of a 1.10 $M_\odot$ sphere of radius R = 37.426 km, starting from a uniform density ($\rho_0 = 10^{13}$ g cm^{-3}) and specific internal energy ($e_0 = 3.64 \times 10^{18}$ ergs g^{-1}) configuration. Once the inner core of the star collapses reaching a central density $\rho_c \approx \rho^\star$, the pressure increases rapidly as the nucleon component causes the EOS to stiffen (Eq. (30)). Following the calculation of May & White (1966), a compression wave suddenly forms close to the center of the star that becomes evident after 6.5×10^{-4} s in the collapse when $\rho_c > 10^{15}$ g cm^{-3} (see their Figs. 2 and 4). The increasing pressure halts the collapse by 7.3×10^{-4} s when $\rho_c \approx 3.0 \times 10^{15}$ g cm^{-3}, which causes the core to bounce, while the outer parts of the star continue to infall at velocities $v/c \leq 0.4$, where c is the speed of light. As a result, the rebounding inner core drives a shock wave outwards reaching the outer layers of the star, reversing the infall and causing an explosive outward motion with a consequent ejection of material.

The initial conditions for this model provide a valuable test for checking the ability of the code to handle the propagation of a shock front in a collapsing medium. A Newtonian approach is justified in this calculation because the relativistic correction terms remain small at least up to 8.0×10^{-4} s, that is, before the shock has had time to reach the surface of the star. Therefore, up to this time the Newtonian calculation should reproduce qualitatively the relevant features of the evolution. Figure 2 displays the resulting density and velocity profiles as a function of the mass μ within a radius r, at distinct times up to 1.08×10^{-3} s. The outward propagation of the shock wave is evident and the details of the evolution compares qualitatively well with those given by May & White (1966) in their Figs. 2 and 4. That is, a compressional wave is evident at about 0.15μ by 6.5×10^{-4} s, and the position of the shock front (with a peak velocity of $\approx 3.2c$) at 7.3×10^{-4} s fairly coincides with that resulting from the fully relativistic calculation. The calculation is halted at 1.08×10^{-3} s when the shock wave has already reached the surface of the star. Although, the Newtonian approach is no longer reliable by this time, the velocity profile of the ejected material still resembles that of the relativistic model with maximum velocities of about $0.70c$.

4. Dynamical evolution of coronal loops

4.1. Non gravity case

MH studied the thermal evolution of coronal loops using time-dependent numerical simulations under the assumption that the inertial terms remain negligible. They considered the effects of spatial variations in the heating and investigated the implications for the formation of cool condensations in a magnetic structure.

In this section, we describe the hydrodynamical evolution of three loop models using the same initial conditions employed by MH and the heating function as given by Eq. (8). All models start with uniform density ($\rho_i = 1.0 \times 10^{-15}$ g cm^{-3}) and temperature ($T_i = 2.0 \times 10^6$ K) profiles and with the same loop length ($s_0 = 2L = 3.0 \times 10^{10}$ cm), differing only in the energy input through the decay-length of the heating (s_H). In order to allow for a direct comparison with MH's isobaric models, here we consider values of $s_* = s_H/L = 10^{81}$, 0.05 and 0.01. A value as high as 10^{81} is used to mimic a uniform heating ($s_H \to \infty$) along the loop. On the other hand, values as low as 0.01 represent models in which the heating is more concentrated at the base of the loop. Following MH, this value is less than the critical value $s_* = 0.043$ below which no equilibrium solution at coronal temperatures is possible. The calculations were made using $n = 50$ grid-zones along half the length of the loop and reflective boundary conditions at the summit ($s = 0$). A constant-pressure boundary condition was applied at the footpoint by keeping there the initial density and temperature unchanged. Calculations with initial grid resolutions corresponding to $n = 100$ and 400 zones, produced essentially the same results compared with the $n = 50$ runs. Thus, working with an initial $n = 50$ grid seems to be enough to accurately describe the evolution for all three models.

In Figs. 3a–c, we show the temperature profiles at different times in the evolution. The sequences shown in Figs. 3a–c correspond to calculations with $s_* = 10^{81}$, 0.05 and 0.01, respectively. In the case of uniform heating (Fig. 3a), the initial isothermal profile evolves towards arcade-like forms with increasing top temperatures. By 4397 s (curve 10), the top temperature reaches a maximum value of 5.72×10^6 K and thereafter the evolution proceeds with the loop temperature distribution oscillating about an equilibrium state as shown by curves 10 to 13. When the value of s_H is lowered to $0.05L$ (Fig. 3b), the evolution proceeds with the top temperature decreasing progressively until it reaches a minimum equilibrium value of 1.86×10^6 K by 36 000 s. In this case, the forms of the temperature profiles are such that the maximum temperature is always located near the footpoint. Note that $s_* = 0.05$ is slightly greater than the critical value of 0.043 above which thermal equilibrium is possible. In this case, the input of energy at the summit is reduced and the balance of energy is established by thermal conduction. Thus, if less energy is supplied into the loop, then the summit temperature is lowered as shown in Fig. 3b. By further decreasing the decay-length of the heating, the system evolves towards much lower summit temperatures. In Fig. 3c, we show the resulting evolution when $s_* = 0.01$. During the first 142 000 s (curves 1 to 5), the top temperature decreases smoothly. Soon after, it suddenly drops down to values of about 7000 K (Fig. 3d and curve 6 of Fig. 3c). At this time, a condensation forms which grows and separates from the rest of the loop by the presence of a shock front behind it. Compared with the previous models, the thermal conduction is now unable to balance the energy losses and so the summit temperature decreases to chromospheric values. After 160 000 s the dense, cool region broadens followed by the appearance of transient humps in the temperature profiles away from the top (curves 9 to 12). The humps arise between 234 000 and 276 000 s as a consequence of a sign reversal of the fluid velocity that leads to a temporary accumulation of mass and energy precisely at their location. By 291 000 s a well-defined condensation has already formed and from this time on (curves 13 to 18), the cool region becomes wider occupying a $0.1s_0$ segment from the top.

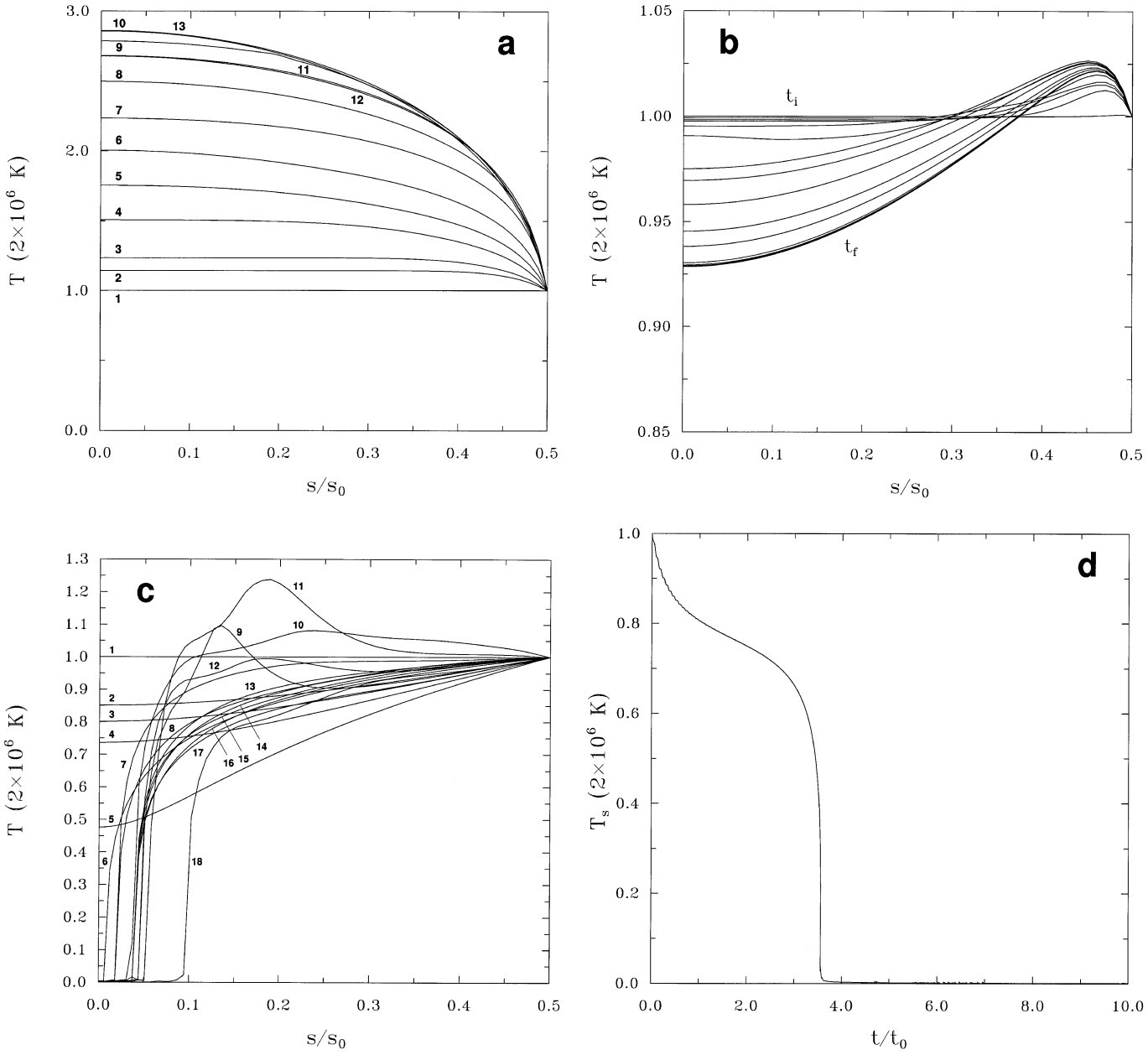

Fig. 3. Temperatures profiles at different times in the evolution of loop models with no gravity, and $s_* = 10^{81}$ **a)**, 0.05 **b)**, and 0.01 **c)**. In each sequence only half of the loop length is shown, with $s_0 = 2L = 3.0 \times 10^{10}$ cm being the total length of the loop. In **a)** the times and summit ($s/s_0 = 0$) temperatures are: 0.0 s, 1.0 (curve 1); 61 s, 1.15 (curve 2); 99 s, 1.24 (curve 3); 212 s, 1.51 (curve 4); 322 s, 1.76 (curve 5); 471 s, 2.01 (curve 6); 829 s, 2.24 (curve 7); 1 297 s, 2.5 (curve 8); 1 865 s, 2.79 (curve 9); 4 397 s, 2.86 (curve 10); 14 865 s, 2.69 (curve 11); 21 141 s, 2.68 (curve 12); and 42 089 s, 2.86 (curve 13), respectively. In **b)** a sequence of times is shown from $t_i = 0$ s to $t_f = 72\,107$ s. An equilibrium summit temperature of 0.93 is reached by 35 901 s. In **c)** the times and summit temperatures for the first six profiles are: 0.0 s, 1.0 (curve 1); 21 701 s, 0.85 (curve 2); 44 454 s, 0.80 (curve 3); 91 536 s, 0.74 (curve 4); 142 237 s, 0.48 (curve 5); and 160 289 s, 3.6×10^{-3} (curve 6), respectively. From curve 7 to 18, the times and summit temperatures go from 200 759 s to 410 494 s and from 2.0×10^{-3} to 7.9×10^{-4}, respectively. Finally, **d)** shows the variation in time of the summit temperature for the same model of **c)**. The time is normalized to $t_0 = 41\,049$ s.

A salient feature of the model evolution displayed in Fig. 3c is the time variability of the temperature loop profile. As the top cools down to chromospheric temperatures (curves 1 to 5), the temperature away from the top also decreases. Once the top temperature reaches chromospheric values (curve 6), the summit temperature varies very little but farther away from the top the plasma heats and thereafter it experiences an increase and decrease in temperature (curves 6 to 13), with strong oscillations (between ~1 MK to ~2.4 MK) occurring within the loop segment $0.1 < s/s_0 < 0.3$. These features have some support from SOHO-CDS observations of coronal loops which seem to undergo strong variability especially in active regions of the solar atmosphere. In particular, Kjeldseth-Moe & Brekke (1998) reported observations of the variability of coronal loop plasma with temperatures ranging from $\sim 10^4$ to $\sim 2.7 \times 10^6$ K. They found clear evidence for rapid time variability in loops

above active regions, i.e., a loop at a given temperature that is missing in one location at a particular time may be present at another time. In the evolution of Fig. 3c, strong oscillations of the temperature occur during a time interval of about 130 000 s which represents no more than 30% of the total evolutionary time. While there is a qualitative similarity with the loop variability observations by Kjeldseth-Moe & Brekke (1998), the timescales reported here are much longer than those (of 10–20 min) observed for rapid evolution of loops by a factor of about 100. A further parametric study possibly starting with higher initial densities might help addressing this quantitative difference in the timescales for rapid loop variability.

For the uniform heating ($s_* = 10^{81}$) case, both the isobaric and the hydrodynamical calculations yield a similar evolution, with the final equilibrium temperature profile having the same form and the top temperature fairly coinciding (see Fig. 3a of MH). One basic difference is that in the hydrodynamical model the final state is not completely stationary but oscillates around an equilibrium value. Similarly, the evolution sequence shown in Fig. 3b for the $s_* = 0.05$ loop closely follows that seen for the isobaric model (see Fig. 3b of MH), with the position of the maximum temperature near the footpoint fairly coinciding in both cases. However, in the hydrodynamical calculation the top is slightly hotter than in the isobaric case due to the mechanical transport of energy from the hotter parts of the loop to the cooler ones. The main differences between the isobaric and the hydrodynamical calculations occur for the $s_* = 0.01$ loop model. One reason for this is that in the isobaric approximation the fluid velocity is always kept much smaller than the local sound speed, and so no supersonic flow can develop along the loop. As a consequence, no transient shock fronts will appear in the solution at the onset of the condensation and so the top cools down with a wide cool segment around it never forming (see Fig. 3c of MH). In the present hydrodynamical case, however, the condensation forms as a result of a shock front which compresses the material around the cool summit. As the condensation grows, the cool region around the summit becomes wider.

A direct inspection of Figs. 3a–c shows that as long as s_* is decreased from 10^{81} to 0.01, the loop evolves towards a final configuration with a cooler summit. This occurs essentially because for lower values of s_*, the initial loop configuration becomes more thermally unbalanced as the heating is more concentrated towards the footpoint region, thereby allowing cooling by radiative losses to dominate over thermal conduction in the top region. When the heating is strongly localized at the footpoint (Fig. 3c with $s_* = 0.01$) such that $s_* < 0.043$, no equilibrium solution at coronal temperatures is possible and a cool condensation necessarily forms at the loop top.

4.2. Gravity case

In a previous work, Mendoza-Briceño (1996) studied the thermal equilibria along a symmetric coronal loop with constant cross-section in the presence of gravity, again using the same heating function as in Eq. (8). He compared the results with those obtained for the constant-pressure models for varying values of the loop length, base heating and decay length of the heating. He found multiple solutions for the above set of space parameters. In particular, he showed that the effect of gravity is just to raise the summit temperature for hot coronal loops above the value obtained for the isobaric models. It was also shown that gravity allows to reach thermal equilibrium states for much lower values of s_H compared with the isobaric case as can be seen from the diagram of Fig. 4. This figure depicts the summit temperature as a function of the base temperature, both in units of 2.0×10^6 K. It can be used as a diagnostic diagram to predict the final hydrostatic equilibrium for given values of the decay length of the loop heating. The plot of Fig. 4 was obtained by solving Eqs. (2) and (3) in the static approximation, i.e., after neglecting the time-dependence of the variables and setting the velocity to zero in both equations (Mendoza-Briceño 1996). The same loop parameters of Sect. 4.1 were used to obtain the curves of Fig. 4. Every point on the curves corresponds to a static solution, while each curve represents a family of solutions. The solid curves refer to the case of constant pressure and the dashed ones to the case with gravity. We may see that including gravity causes the turning point to be shifted to the left side of T_b, where thermal equilibrium is found for prescribed values of the base temperature (Mendoza-Briceño & Hood 1997). For instance, for $T_b = 1.0$ and $s_* = 0.01$, no equilibrium solution is found when gravity is zero but when it is included there exist two possible solutions. For $s_* = 0.05$ the two solutions are shifted: the hot one to a higher value and the cool one to a lower value of the summit temperature. Thus, in the presence of gravity smaller values of s_* are necessary to reach a critical value below which no hot solutions exist. In other words, under hydrostatic equilibrium

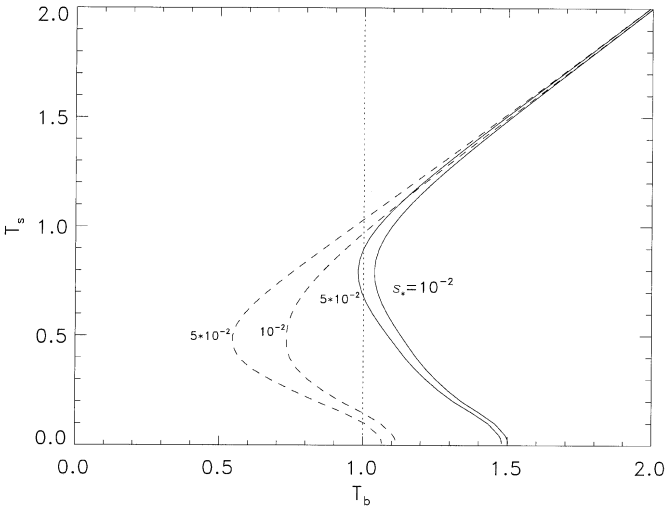

Fig. 4. The summit temperature T_s as a function of the base temperature T_b for two values of the decay length of the heating $s_* = s_H/L$. The solid and dashed lines show families of solutions with no gravity and with gravity, respectively. The dotted line indicates the base temperature used in the calculations. Note that both T_s and T_b are in units of 2.0×10^6 K. The curves shown correspond to thermal equilibrium solutions coupled with a constant-pressure condition (non-gravity case) and a hydrostatic-equilibrium condition (gravity case).

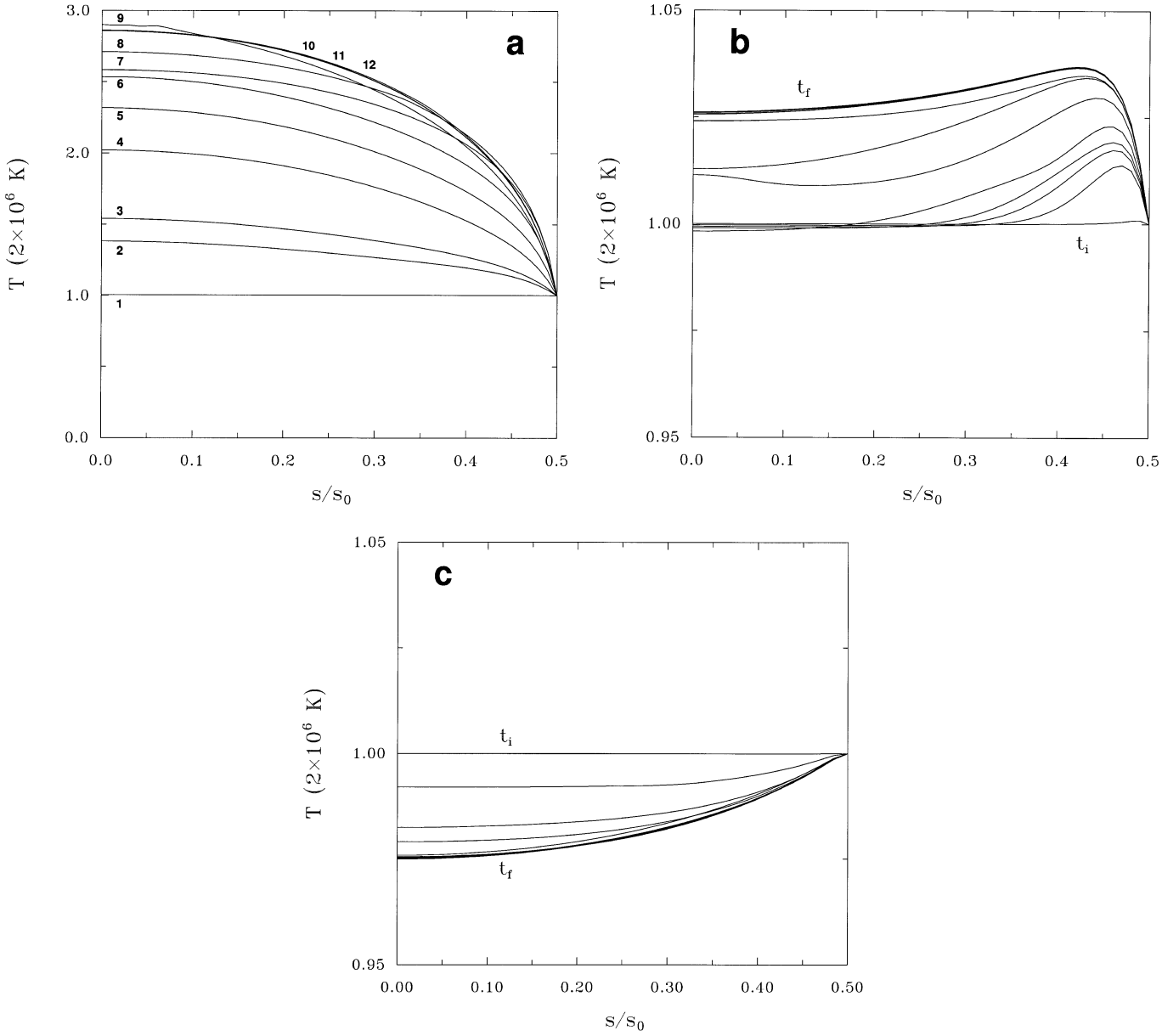

Fig. 5. Temperatures profiles at different times in the evolution of loop models with gravity, and $s_* = 10^{81}$ **a)**, 0.05 **b)**, and 0.01 **c)**. In each sequence only half of the loop length is shown, with $s_0 = 2L = 3.0 \times 10^{10}$ cm being the total length of the loop. In **a)** the times and summit ($s/s_0 = 0$) temperatures are: 0.0 s, 1.0 (curve 1); 64 s, 1.38 (curve 2); 93 s, 1.54 (curve 3); 197 s, 2.02 (curve 4); 292 s, 2.32 (curve 5); 421 s, 2.54 (curve 6); 747 s, 2.59 (curve 7); 1186 s, 2.71 (curve 8); 1745 s, 2.90 (curve 9); 4271 s, 2.86 (curve 10); 14 746 s, 2.86 (curve 11); and 21 030 s, 2.86 (curve 12), respectively. In **b)** a sequence of times is shown from $t_i = 0$ s to $t_f = 68\,942$ s. An equilibrium summit temperature of 1.026 is reached by 34 485 s. In **c)** a sequence of times is shown from $t_i = 0$ s to $t_f = 192\,140$ s. An equilibrium summit temperature of 0.98 is reached by 8 323 s.

the pressure falls off with height making the equilibrium move farther away from the line $T_b = 1.0$.

In this section, we first describe the results obtained by recalculating the above loop models by including the effects of the solar gravity. The gravity term is as given by Eq. (5). As in Sect. 4.1, the models start with a uniform temperature ($T_i = 2.0 \times 10^6$ K) profile and with a total length of 3.0×10^{10} cm. With this assumption, the initial density profile is obtained by setting the initial velocity to zero and solving the equation of hydrostatic equilibrium through the use of the EOS (4). Figures 5a–c show the temperature profiles at different times during the evolution of models with $s_* = 10^{81}$, 0.05 and 0.01, respectively. We note from Fig. 5a that for uniform heating the evolution is quite similar to the non-gravity model (Fig. 3a), with the exception that the equilibrium is reached at a slightly higher top temperature. The occurrence of a higher temperature in the presence of gravity can be interpreted in terms of the above discussion on the diagram of Fig. 4. The effects of gravity are made more evident in Figs. 5b and c, which displays the evolution for the $s_* = 0.05$ and 0.01 cases, respectively. In particular, looking at Fig. 5b we see that the equilibrium profile is obtained at a higher top temperature compared

to the non-gravity case (Fig. 3b). The difference between gravity and non-gravity models becomes even more significant for $s_* = 0.01$, where now catastrophic cooling of the top is never attained as shown in Fig. 5c. These results are in close agreement with the predictions made by Fig. 4. Of the two possible solutions, all models are seen to evolve towards the hotter one, which also corresponds to the most stable state. For a base temperature $T_b = 1.0$, corresponding to 2.0×10^6 K, the hotter solution in Fig. 4 predicts at equilibrium a summit temperature slightly above $T_s = 1.0$ for $s_* = 0.05$ and slightly below $T_s = 1.0$ for $s_* = 0.01$, which agrees with the equilibrium values of $T_s = 1.026$ and 0.98 obtained for the $s_* = 0.05$ and $s_* = 0.01$ hydrodynamical models, respectively.

The inclusion of gravity causes the loop top regions to attain lower densities compared to the non-gravity models. Since the radiative loss term in Eq. (6) is proportional to ρ^2, a lower density will act all the way to reduce the effects of cooling by radiative losses. As a consequence, the loop evolves towards a final equilibrium configuration with a hotter top region and the threshold value of s_* for a condensation to form is lowered. This means that in the presence of gravity the heating must be even more localized than has been tried in the present models in order to form a cool condensation at the loop top.

Recently, Aschwanden et al. (2001) calculated hydrostatic solutions for symmetric loops in steady-state equilibrium and fitted their solutions to observed fluxes of EUV loops. They found that none of the EUV loops can be fitted with models of uniform heating ($s_* \to \infty$) or loop top heating and that only heating functions localized within the 10–20 Mm near the loop footpoints (i.e., for $s_* = 0.22 \pm 0.11$) fit about 30% of the observed loops. In particular, the results of Fig. 5b are in close agreement with the essential hallmarks of the hydrostatic solutions with localized heating reported by Aschwanden et al. (2001), namely, that the resulting equilibrium temperature profile is near-isothermal in its coronal segments with the maximum temperature occurring away from the loop top, that the maximum pressure is always located at the loop base and that the density scale heights are effectively longer compared to the uniform heating model of Fig. 5a. Because of the much lower heating scale length ($s_* = 0.05$) used here compared to the value of $s_* = 0.22 \pm 0.11$ found by Aschwanden et al. (2001), the above correspondence is not direct. Values of the decay length higher than $s_* = 0.05$ are expected to produce final equilibrium temperature profiles which are near-isothermal in their coronal segments and with the maximum temperature shifted towards an intermediate location between the top and the footpoint. Furthermore, if the heating were considered to be variable in time as could probably be the case in the solar atmosphere, the decay length of the heating could be modified. In this way, those loops which could appear to be in a steady-state configuration at some particular time could become more dynamic and hence evolve towards a new equilibrium in another time.

The results of Fig. 5 clearly shows that decreasing s_*, while keeping h_0 and L fixed, produces a final structure with decreasing top temperatures. Thus, compared to the non-gravity models, the inclusion of gravity lowers the threshold value of s_* below which no hot solutions exist. Variations of the initial density and temperature may also influence the threshold value of s_* because a lower density will decrease the effects of radiative cooling while lower temperatures will work towards increasing these effects. On the other hand, variations of the loop length L and the heat deposition h_0 may also result in a shift

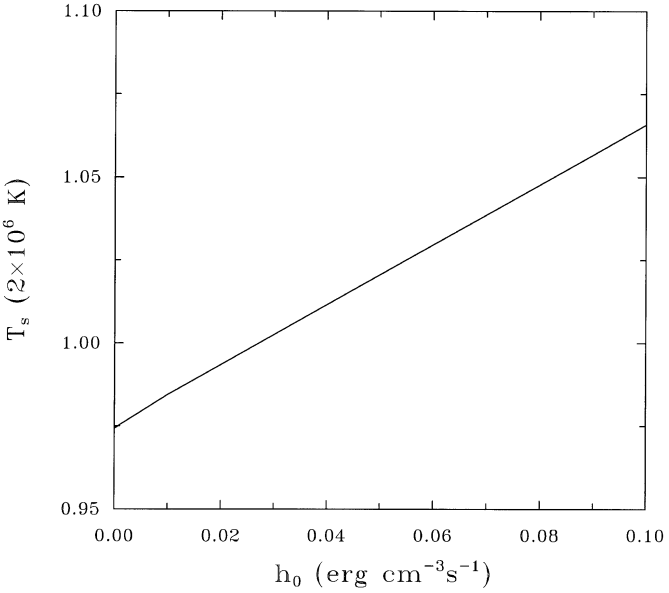

Fig. 6. Dependence of the final equilibrium top temperature T_s on heat deposition h_0 as obtained from the hydrodynamical evolution of seven loop models (with gravity) starting with a uniform temperature ($T_i = 2.0 \times 10^6$ K) profile and a hydrostatic density stratification. This sequence of models have $s_* = 0.01$, $s_0 = 2L = 3.0 \times 10^{10}$ cm and varied heat deposition h_0 with values of 10^{-4}, 5×10^{-4}, 10^{-3}, 5×10^{-3}, 10^{-2}, 5×10^{-2}, and 0.1 erg cm^{-3} s^{-1}, respectively.

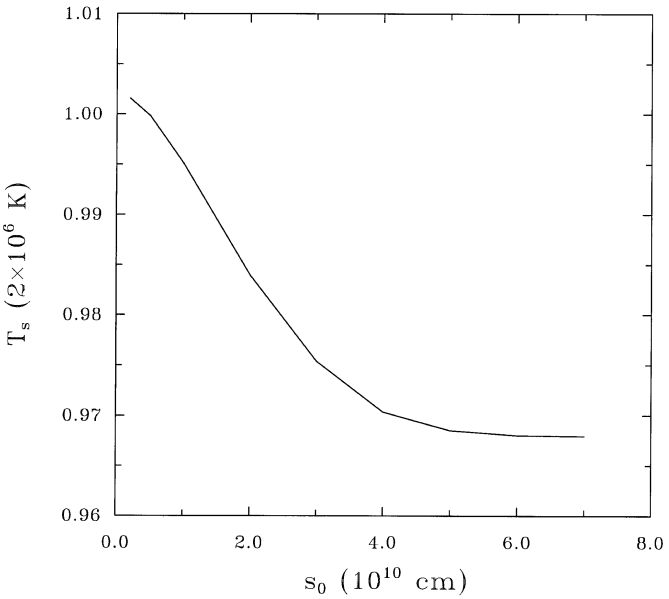

Fig. 7. Dependence of the final equilibrium top temperature T_s on total loop length $s_0 = 2L$ as obtained from the hydrodynamical evolution of nine loop models (with gravity) starting with a uniform temperature ($T_i = 2.0 \times 10^6$ K) profile and a hydrostatic density stratification. This sequence of models have $s_* = 0.01$, $h_0 = 10^{-3}$ erg cm^{-3} s^{-1} and varied $s_0/10^{10}$ cm with values of 0.2, 0.5, 1, 2, 3, 4, 5, 6 and 7, respectively.

of the threshold value of s_*. Whereas a study of the effects of varying all these parameters is beyond the scope of this paper, here we shall only explore the effects of varying h_0 and L along two separate sequences of model calculations with gravity. According to Eq. (9), if s_* is fixed, the total power of heat input will vary along both sequences. In particular, Fig. 6 shows the dependence of the final top temperature on h_0 for seven loop models starting with $s_* = 0.01$, $s_0 = 2L = 3\times10^{10}$ cm and varied h_0 from 10^{-4} to 0.1 erg cm^{-3} s^{-1}. In all cases, the evolution is quite similar to that displayed in Fig. 5c. We see that the final equilibrium top temperature increases with increasing h_0. This occurs because as h_0 is increased more energy is supplied to the system, leading to a hotter loop configuration. The results of varying the loop length with h_0 and s_* fixed are shown in Fig. 7, which displays the dependence of the resulting top temperature on total loop length $s_0 = 2L$ for nine model calculations all starting with $s_* = 0.01$, $h_0 = 10^{-3}$ erg cm^{-3} s^{-1} and s_0 varying from 2×10^9 to 7×10^{10} cm. The evolution towards an equilibrium structure is again similar to that shown in Fig. 5c. As long as the loop length increases, the top temperature decreases monotonically due to thermal conduction becoming progressively less efficient as L is increased. We note that for the chosen values of s_* and h_0, heat conduction is more important for $s_0 \le 4\times10^{10}$ cm as shown by the more rapid decline of T_s within this length interval. For $s_0 > 4\times10^{10}$ cm, the top temperature becomes a constant function of s_0, implying that heat conduction plays no role for such great lengths. Evidently, the fact that varying h_0 or L produces different final summit temperatures means that the threshold value of s_* is also affected by these variations. Varying s_* and h_0 such that H_t remains constant while keeping the base temperature fixed at 2×10^6 K will result in higher top temperatures, with the trends of the evolution being, however, similar to those seen for the non-constant H_t sequences.

We may still use Fig. 4 to find a region of the parameter space (s_*, h_0, L) where thermal equilibria at coronal temperatures can no longer be found. An easy way of finding such solutions is by lowering the boundary temperature T_b of the loop model. In particular, if T_b is reduced to 0.5 (corresponding to 10^6 K), the threshold value of s_* for a cool condensation to form should be around 0.05 according to the predictions of Fig. 4. In order to check this point, we define a sequence of seventeen loop model calculations (with gravity) this time starting with a uniform temperature profile at 10^6 K, fixed values of h_0 (=10^{-3} erg cm^{-3} s^{-1}) and $s_0 = 2L$ (=3.0×10^{10} cm) and varying decay length of the heating from 6.67×10^{-3} to 1.0. Figure 8 shows the dependence of the summit temperature, as obtained at the end of the hydrodynamical evolutions, on s_*. We see that thermal equilibrium solutions with coronal temperatures are possible for decay lengths greater than the critical value $s_* = 0.0553$. For lower values the final temperature drops to chromospheric values with a cool condensation forming at the loop top. The details of the evolutions leading to a cool top condensation are similar to those shown in Fig. 3c for the non-gravity case, while those ending with a hot summit at equilibrium (for $s_* > 0.0553$) resemble the profiles of Fig. 5b. We also note from Fig. 8 that as long as s_* is gradually decreased the final equilibrium top temperature also decreases.

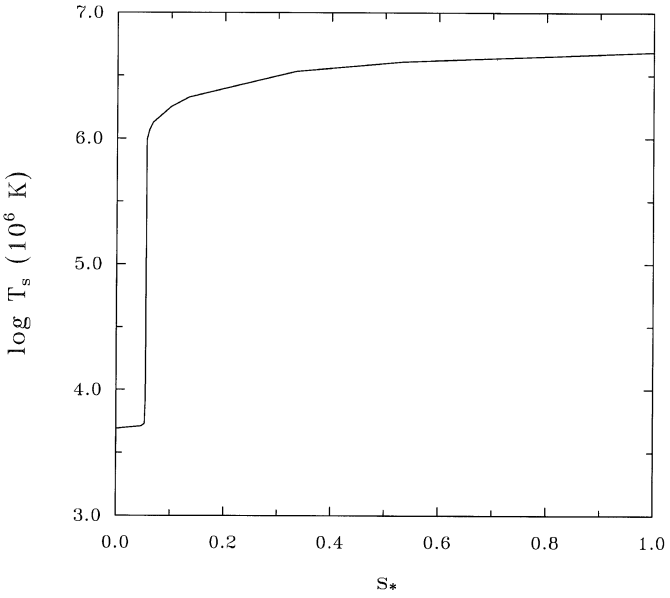

Fig. 8. Dependence of the final equilibrium top temperature T_s on the decay length of the heating s_* as obtained from the hydrodynamical evolution of seventeen loop models (with gravity) starting with a uniform temperature ($T_i = 10^6$ K) profile and a hydrostatic density stratification. This sequence of models has $h_0 = 10^{-3}$ erg cm^{-3} s^{-1}, $s_0 = 2L = 3\times10^{10}$ cm and varied s_* with values between 6.67×10^{-3} and 1.0.

This effect becomes more pronounced when the decay length of the heating approaches the critical value $s_* = 0.0553$. Below this value the coronal loop experiences a catastrophic cooling and a condensation forms. Such thermal instability arises in a way similar to the case of Fig. 3c because for strongly localized energy sources the thermal conduction is unable to balance the radiative losses at the loop top causing a drop of the temperature. The sequence of model calculations in Fig. 8 shows that when the loop is started with a reduced base temperature, the threshold value of s_* raises.

5. Conclusions

In this paper, we have performed hydrodynamical calculations of the evolution of coronal loop models. The calculations were made using a Lagrangian-remap code based on an extension of the scheme proposed by Lufkin & Hawley (1993) to include the effects of thermal conduction and radiative losses. The scheme has been extensively tested on a wide variety of tests in order to validate its accuracy and robustness. In particular, the dynamical evolution of coronal loop models has been investigated here for varying decay length of the heating s_H, varying heat deposition at the base of the loop and varying total loop length, using a form of the heating function that depends on distance along the loop. The initial and boundary conditions for the calculations were chosen to allow for a direct comparison with previous isobaric calculations (Mendoza & Hood 1996) and to quantify the

effects of including the gravity term. The main conclusions can be summarized in the following points:

(i) On varying the decay length of the heating from $s_* = 10^{81}$ (case of uniform heating along the loop) to the value $s_* = 0.01$ (case in which the heating is concentrated at the footpoint), the models reach final states with decreasing temperature at the apex. This conclusion is equally valid for models with and without gravity, respectively.

(ii) For all cases studied here, when gravity is included the final equilibrium profiles tend to be hotter than those obtained when gravity is neglected. In the latter case, a cool condensation forms for $s_*(= 0.01)$ below the threshold value of 0.043. The inclusion of gravity lowers this threshold value, thereby producing a final equilibrium loop with a hot apex when $s_* = 0.01$.

(iii) There are no significant differences between the isobaric and hydrodynamical models for sufficiently hot loops, i.e., for values of the decay length of the heating larger than about 0.05. The dynamical effects are seen to become important only for values of s_* as low as 0.01.

(iv) It is possible to predict the final summit equilibrium temperature reached by the hydrodynamical loop models using the diagram of Fig. 4, which describes for given values of the base temperature and decay length of the heating the location of the allowed family of equilibrium solutions.

(v) The above results clearly indicates that the inclusion of gravity lowers the threshold value of s_* for a condensation to form. The same is true for variations of the heat deposition h_0 and total length L of the loop. In particular, loop models with varying h_0 and fixed s_* and L evolves towards equilibrium structures with higher top temperatures as h_0 is increased. On the other hand, loops with varying total length evolves towards lower top temperatures as L is increased. When the loop model is started with a reduced base temperature, the threshold value of s_* raises.

(vi) The existence of critical values in the parameter space, as shown here for s_*, for which hot plasma ceases to exist, suggests that catastrophic cooling leads to the formation of cool condensations. Further work should be done to relate this process with the formation of prominence-like structures.

(vii) While the present models started from rather unrealistic initial conditions (i.e., uniform density and temperature for the non-gravity models and uniform temperature for the gravity cases), they represented valuable tests to check the ability of the hydrodynamic code to reproduce the general trends predicted by previous isobaric and hydrostatic models. A drawback of using uniform initial conditions is that they strongly overemphasize the effects of radiative cooling at the loop top as the cooling accelerates in the course of the thermal instability. Therefore, the predictions made in this paper could be quantitatively modified if more realistic initial conditions are used. Further work in this line will concentrate on employing initial hydrostatic stratifications along with a more complete parametric study.

Acknowledgements. We thank the referee for providing a number of helpful suggestions and comments that have improved the presentation and quality of the manuscript. One of us (C. A. M-B.) would like to thanks the CDCHT of the Universidad de los Andes for financial support and the Fonacit for the support through its Programme of Pasantias Postdoctorales. The calculations of this paper were made using the computational facilities of the Laboratory of Computational Physics at the IVIC Center of Physics.

References

Antiochos, S. K., MacNeice, P. J., Spicer, D. S., & Klimchuk, J. A. 1999, ApJ, 512, 985
Aschwanden, J. M., Schrijver, C. J., & Alexander, D. 2001, ApJ, 550, 1036
Bader, G., & Deuflhard, P. 1983, Numerische Mathematik, 41, 373
Bae, S.-H., & Lahey, R. T. 1999, J. Comput. Phys., 153, 575
Braginskii, S. I. 1965, Rev. Plasma Phys., 1, 205
Bray, R. J., Cram, L. E., Durrant, C. J., & Loughead, R. E. 1991, Plasma Loops in the Solar Corona (Cambridge: Cambridge Univ. Press), 293
Brown, S. F. 1996, A&A, 305, 649
Hildner, E. 1974, Sol. Phys., 35, 23
Hood, A. W., & Anzer, U. 1988, Sol. Phys., 115, 61
Hood, A. W., & Priest, E. R. 1979, A&A, 77, 233
Kjeldseth-Moe, O., & Brekke, P. 1998, Sol. Phys., 182, 73
Klimchuk, J. A. 1987, ApJ, 323, 368
Klimchuk, J. A., & Mariska, J. T. 1988, ApJ, 328, 334
Landini, M., & Landi, E. 2002, A&A, 383, 653
Lenz, D. D., Deluca, E. E., Golub, L., Rosner, R., & Bookbinder, J. A. 1999, ApJ, 517, L155
Lufkin, E. A., & Hawley, J. F. 1993, ApJS, 88, 569
Mariska, J. T. 1987, ApJ, 319, 465
May, M. M., & White, R. H. 1966, Phys. Rev., 141(4), 1232
Mendoza-Briceño, C. A. 1996, Ph.D. Thesis, University of St. Andrews, St. Andrews, Scotland
Mendoza, C. A., & Hood, A. W. 1996, Astro. Lett. and Communications, 34, 107 (MH)
Mendoza-Briceño, C. A., & Hood, A. W. 1997, A&A, 325, 791
Mok, Y., Drake, J. F., Schnack, D. D., & van Hoven, G. 1990, ApJ, 359, 228
Nightingale, R. W., Aschwanden, M. J., & Hurlburt, N. E. 1999, Sol. Phys., 190, 249
Noh, W. F. 1987, J. Comput. Phys., 72, 78
Oluseyi, H. M., Walker, A. B. C., Santiago, D. I., Hoover, R. B., & Barbee, T. W. 1999, ApJ, 527, 992
Parker, E. N. 1988, ApJ, 330, 380
Peres, G. 2000, Sol. Phys., 193, 33
Press, W. H., Teukolsky, S. A., Vetterling, W. T., & Flannery, B. P. 1992, Numerical Recipes (Cambridge University Press, Cambridge), 735
Reale, F., Peres, G., Serio, S., et al. 2000, ApJ, 535, 423
Rosner, R., Tucker, W. H., & Vaina, G. S. 1978, ApJ, 220, 643
Sarro, L. M., Erdélyi, R., Doyle, J. G., & Pérez, M. E. 1999, A&A, 351, 721
Serio, S., Peres, G., Vaiana, G. S., Golub, L., & Rosner, R. 1981, ApJ, 243, 288
Sigalotti, L. di G., & Klapp, J. 2001, IJMP D, 10(2), 115
Sod, G. A. 1978, J. Comput. Phys., 27, 1
Steele, C. D. C., & Priest, E. R. 1994, A&A, 292, 291
Strong, K. T. 1994, Proc. of Kofu Symp., NRO Report 360, 53
Teriaca, L., Doyle, J. G., Erdélyi, R., & Sarro, L. M. 1999, A&A, 352, L99
Tsuneta, S. 1993, In ESA, Fourth International Tokyo Conference on Plasma Physics and Controlled Nuclear Fusion, 75
van Leer, B. 1977, J. Comput. Phys., 23, 263
Vesecky, J. F., Antiochos, S. K., & Underwood, J. H. 1979, ApJ, 233, 987